

See discussions, stats, and author profiles for this publication at: <https://www.researchgate.net/publication/305517340>

Monitoring CO₂ invasion processes at the pore scale using Geological Labs on Chip

Article in Lab on a Chip · July 2016

DOI: 10.1039/C6LC00830E

CITATIONS

30

READS

231

7 authors, including:



Sandy Morais

Institut de Chimie de la matière condensée de Bordeaux

11 PUBLICATIONS 113 CITATIONS

SEE PROFILE



Na Liu

University of Bergen

22 PUBLICATIONS 244 CITATIONS

SEE PROFILE



Abdou Diouf

Institut de Chimie de la matière condensée de Bordeaux

4 PUBLICATIONS 31 CITATIONS

SEE PROFILE



Carole Lecoutre

French National Centre for Scientific Research

105 PUBLICATIONS 1,008 CITATIONS

SEE PROFILE

Some of the authors of this publication are also working on these related projects:



Phase Separation in Microgravity [View project](#)



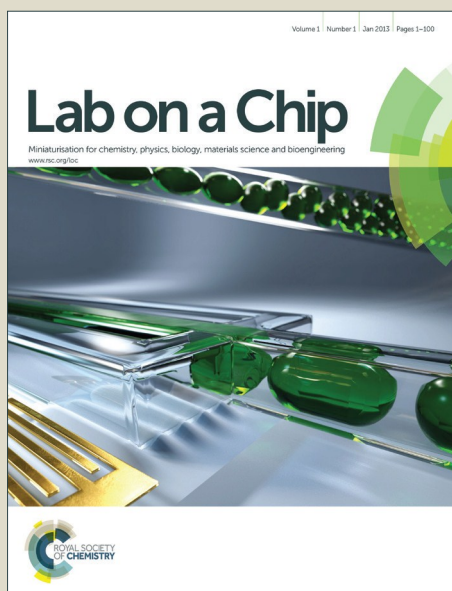
IMMENS Improving microbial selective plugging technology through experimentally based modelling and simulation [View project](#)

Lab on a Chip

Accepted Manuscript



This article can be cited before page numbers have been issued, to do this please use: S. Morais, N. Liu, A. Diouf, D. Bernard, C. Lecoutre, Y. Garrabos and S. MARRE, *Lab Chip*, 2016, DOI: 10.1039/C6LC00830E.



This is an *Accepted Manuscript*, which has been through the Royal Society of Chemistry peer review process and has been accepted for publication.

Accepted Manuscripts are published online shortly after acceptance, before technical editing, formatting and proof reading. Using this free service, authors can make their results available to the community, in citable form, before we publish the edited article. We will replace this *Accepted Manuscript* with the edited and formatted *Advance Article* as soon as it is available.

You can find more information about *Accepted Manuscripts* in the [Information for Authors](#).

Please note that technical editing may introduce minor changes to the text and/or graphics, which may alter content. The journal's standard [Terms & Conditions](#) and the [Ethical guidelines](#) still apply. In no event shall the Royal Society of Chemistry be held responsible for any errors or omissions in this *Accepted Manuscript* or any consequences arising from the use of any information it contains.



Lab on a Chip

ARTICLE

Monitoring CO₂ invasion processes at pore scale using Geological Labs on Chip

S. Morais[†], N. Liu[†], A. Diouf, D. Bernard, C. Lecoutre, Y. Garrabos, S. Marre^{*}

Received 00th January 20xx,
Accepted 00th January 20xx

DOI: 10.1039/x0xx00000x

www.rsc.org/

In order to investigate at pore scale the mechanisms involved during CO₂ injection in a water saturated pore network, a series of displacement experiments is reported using high pressure micromodels (Geological Labs on Chip – GloCs) working in real geological conditions (25 < T (°C) < 75 and 4.5 < p (MPa) < 8). The experiments were focused on the influence of three experimental parameters: (i) the p,T conditions, (ii) the injection flowrates and (iii) and the pore networks characteristics. By using on chip optical characterization and imaging approaches, the CO₂ saturation curves as a function of either the time or the number of pore volume injected were determined. Three main mechanisms were observed during CO₂ injection, namely: invasion, percolation and drying, which are discussed in this paper. Interestingly, besides conventional mechanisms, two counterintuitive situations were observed during the invasion and the drying processes.

Introduction

The sustainable management of anthropogenic CO₂ emissions is currently a key factor for stabilizing the global atmospheric content of this greenhouse gas.¹ Carbon dioxide capture and storage (CCS) is planned to be performed at large scale, and remains an appropriate long-term option for reducing its concentration in the atmosphere. CO₂ can typically be stored in deep geological formations (carbon Geological Storage – CGS) at depths below one kilometre, including unmineable coal beds, depleted oil and gas reservoirs or deep saline aquifers,^{2, 3} where the typical conditions in temperature and pressure are in the range 30–80°C and 6–20 MPa. This latter option of geological formation is by far the most promising one in term of estimated storage capacity (≈ 10,000 Gt of CO₂).⁴ Deep saline aquifers consist of permeable deep sedimentary rocks saturated with formation waters or brines containing high concentrations of dissolved salts, and covered by a caprock exhibiting a very low permeability.⁵

Mechanisms of CO₂ storage in deep saline aquifers. The successful sequestration of carbon dioxide is globally governed by different fluid-fluid and fluid-rock interactions. When CO₂ is injected into deep saline aquifers, four physicochemical mechanisms cause it to remain trapped physically (*structural* and *capillary trapping*) or chemically (*solubility trapping*)

followed by eventual *mineral trapping* through solid carbonates precipitation).⁶ Consequently, this kind of storage requires adequate scientific knowledge to evaluate injection scenarios, to estimate reservoir capacity and to assess leakage risks.

The evolution of the CO₂/brine phase distribution within the reservoir, including displacement stability, fluid flow pathways and pore saturation levels,⁷ is a key parameter to be determined to estimate the true storage capacity of the aquifer as well as the stability of the stored volume. These processes are influenced by a large number of parameters such as fluid viscosity and density, interfacial tension,⁸ wetting properties, topography and geological features of the reservoir,^{9, 10} and CO₂ flow rates.¹¹

Most of the investigations of subsurface processes in geological formations are described at reservoir scale, requiring averaged properties and processes, the physicochemical processes take place in discontinuous pore geometries and are controlled by interface processes, which ultimately require a pore-scale view for achieving fine mechanisms understanding. Therefore, to achieve this fine resolution, lab scale tools are needed to be able to screen, to separate and to follow step-by-step such processes at the selected resolution. To investigate these questions, geologists generally use core scale experiments to characterize the CO₂ invasion process in brine, thus limiting the fast screening.¹² This statement is correlated to the lack of adapted experimental means integrated with various *in situ* characterization techniques. In this context, microfluidics tools can address part of these limitations.

Micromodels and Geological Labs on Chip. Indeed, for more than 20 years, microfluidics has advanced biological,^{13, 14}

[†]These two authors equally contributed to this work

^{*}CNRS, Univ. Bordeaux, ICMCB, F-33600, Pessac France. Email:

samuel.marre@icmcb.cnrs.fr

[†]Electronic Supplementary Information (ESI) available: [details of any supplementary information available should be included here]. See DOI: 10.1039/x0xx00000x

chemical¹⁵⁻¹⁷ and materials¹⁸ research. Formerly limited to the normal conditions of pressure and temperature, the use of microreactors was recently extended to high pressures and high temperatures (HP/HT) conditions,¹⁹ which can constitute a chance to take advantage of microfluidics strategies for studying, in real conditions, the phases equilibria²⁰ and the hydrodynamics processes occurring deep underground. Model porous media on chip can be easily designed through the flexible photolithography fabrication process to simulate pore networks - their characteristics can be made similar to those encountered in sedimentary aquifers. Several studies have been reported concerning the use of porous microsystems ("micromodels") for studying fluids displacements in porous media made either of PDMS (Polydimethylsiloxane) or glass-glass (non-reactive)²¹⁻²⁴ or directly etched within real rocks materials (reactive).²⁵ These were initially mostly dedicated to the investigation of Enhanced Oil Recovery topics considering oil, aqueous phases or foams.²⁶ However, only very few recent examples have been reported by our team and others concerning the use of HP/HT micromodels made of silicon and Pyrex for mimicking the real temperature and pressure conditions in which CO₂ geological storage-related mechanisms happen at large depths.^{22, 23, 27-29} These experimental tools allow a direct visualization of the two phases and therefore the pore-scale fluid distribution and displacement. Indeed, the Geological Labs on Chip (GLoCs) provide the possibility to inject CO₂ at geological (p,T) conditions, into a water-saturated micro porous media, consisting in pore network patterns etched into silicon.³⁰

Based on the above-mentioned considerations, we are presenting in this paper a series of two-phase fluid flow experiments performed in a well-designed pore network inside high-pressure silicon/Pyrex micromodels. The micromodels do not aim at representing an entire reservoir, but rather aim at investigating some flow situations at different locations of a reservoir (close/far from the injection well). Therefore, by considering only a small portion of the geological formation, the CO₂ can flow through the considered section of pore network volume. The non-reactive pore network models used in here are "simple" compared to real geological porous materials. Nevertheless, this approach remains representative of the hydrodynamics mechanisms encountered in more realistic porous media. In here, the non-reactive pore networks were visualized during the drainage experiments to capture in particular some of the key flowing and storage mechanisms of the CO₂ invasion at pore scale, namely: invasion, percolation and drying, as a function of the pore size, the p and T conditions and the injection flowrate. The idea is to take advantage of two main characteristics of their quasi-2D geometry to observe in real (p,T) conditions, the behaviour of the two phase distribution at different operating conditions. First, their small vertical dimension – typically 10 times smaller than the lateral ones – makes it possible to visualize the water-CO₂ interfaces by neglecting the interface curvature along the thickness of the meniscus. These 2D top views can therefore be used (i) to discern the fluid configurations and the invasion

behaviours, including counterintuitive ones concerning the interface curvatures and (ii) to visualize the evolution of the wetting layers, which could strongly impact the drying dynamic. The second main interest of these micromodels is to access pressure drops values – similarly to conventional core scale experiments – but also to benefit from visual characterizations allowing getting quantitative information such as the saturation values as a function of the number of pores volumes injected (NPV), which cannot be accessed with conventional 3D core scale experiments besides considering specific X-rays imaging techniques.³¹

Material and methods

Microfabrication. The GLoCs were fabricated using standard photolithography / wet etching of silicon followed by anodic bonding to a Pyrex wafer (section S1 in the ESI).^{18, 19, 32} Several strategies were already employed to design adapted pore networks structures.^{7, 28, 33, 34} In here, The GLoCs design was specifically made for real pressure conditions experiments. It consists in a simple pore network design made of a staggered plot pattern following a triangular pavement, one side in the transverse direction to the mean flow direction, starting with an ideal 1286 plots mask in a patterned area of 20,2 × 5 mm² (L × w), 78 plots (transverse) lines, 16.5 plots (longitudinal) staggered lines (Fig. 1-A). The staggered characteristic wavelength of the mask was $\lambda = 300 \mu\text{m}$. The circular plot diameter of the mask is $d_M = 250 \mu\text{m}$. The mask porosity can therefore be calculated by (Eq.1):

$$\phi = 1 - \frac{d_M^2}{2\lambda^2 \times \sqrt{3}} = 0.37 \quad (\text{Eq. 1})$$

To ensure an initial penetrating CO₂ front homogeneity, the pore network was sandwiched between two "adaptive parts" consisting of 8 microchannels and a hydrodynamic buffered zone of 500 μm in width (Fig. 1).

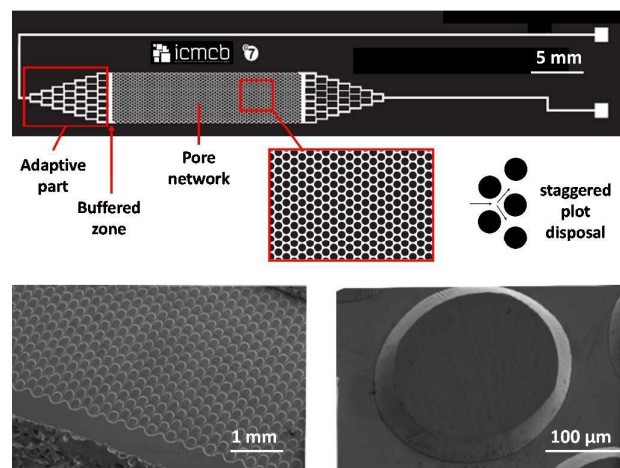


Fig. 1. Design of the Geological Lab on Chip used in this study with additional SEM images of a wet etched porous media.

Two types of GLoCs with different depth and pore network characteristics were used in this study (Table 1). The variation of the porosity compared to the original 2D mask is due to the

wet etching process in the third dimension. The depth was measured with a profilometer (Veeco Dektak) showing a variation of ± 200 nm over the full-etched area, while the lateral resolution was ± 3 μm (from SEM pictures). The surface wettability was not modified, leading to hydrophilic micromodels (water is the wetting fluid). The wetting contact angle (θ) was experimentally measured from pictures of water / CO_2 interface within a straight microchannel at various operating (p,T) conditions (see section S2 in ESI). Unlike the traditional dry-etching DRIE approach, wet etching does not lead to smooth vertical walls, but creates heterogeneities at the micrometres scale, which raise particular fluids behaviour hardly discussed in former experimental / numerical modelling studies.

Table 1. Geometrical characteristics of the two different fabricated GLoCs considered in the present work.

	M1	M2
Depth - d (μm)	22.3 ± 0.2	17.5 ± 0.2
Length - L (μm)	20000	20000
Width - w (μm)	5000	5000
Plots mean diameter (μm)	235 ± 3	229 ± 3
Pore body (μm)	279 ± 3	287 ± 3
Pore throat (μm)	62 ± 3	67 ± 3
Porosity - ϕ (%)	44.3 ± 0.8	46.6 ± 0.9
Total cross section area - A_T (μm^2)	111500	87500
Total pore network volume - V_T (μL)	2.23 ± 0.02	1.75 ± 0.02

Parameters of interest. Among the various input parameters, which can influence the CO_2 invasion process in an aqueous phase saturated pore network, the interfacial tension and the wettability display strong influence on the CO_2 capillary breakthrough pressure (p_c , given by the Laplace equation – Eq. 2) and consequently highly affect the flow patterns by controlling the capillary-sealing efficiency.³⁵

$$p_c = \frac{2 \gamma_{w,\text{CO}_2} \cos \theta}{R} \quad (\text{Eq. 2})$$

where γ_{w,CO_2} is the CO_2 /brine interfacial tension, θ is the CO_2 /water/solid surface contact angle and R is the radius of the largest pore throat that is accessible to CO_2 /brine interface.

The drainage or imbibition processes results from a competition between viscous and capillary forces. It is convenient to considered two parameters: the capillary number for small scale environment (Ca , Eq.3)²⁴ and the viscosity ratio (M , Eq.4). The first one relates viscous to capillary forces through the equation:

$$Ca = \frac{\mu_{\text{CO}_2} u_{\text{CO}_2}}{\gamma_{w,\text{CO}_2} \cos \theta} \quad (\text{Eq. 3})$$

where μ_{CO_2} and u_{CO_2} are the viscosity and the average velocity of the invasive non-wetting fluid, respectively and γ_{w,CO_2} is the water – CO_2 interfacial tension.

The second one represents the viscosity ratio between the wetting and the invading phase, respectively:

$$M = \frac{\mu_{\text{nw}}}{\mu_{\text{w}}} \quad (\text{Eq. 4})$$

Overall, the competition between capillary and viscous forces impacts the pathways of the injected fluid and the most

important output parameter, which is the time dependent saturation of the porous media, is defined as (Eq.5):

$$S(t) = \frac{V_{\text{CO}_2}(t)}{V_T \times \phi} \quad (\text{Eq. 5})$$

Where V_{CO_2} is the pore volume occupied by CO_2 at injection time t , V_T is the total pore network volume and ϕ is the porosity.

Set-up and drainage/imbibition experiments. The micromodels were integrated within a larger set-up (Fig. 2). An injection part based on the compression of O-rings ensures a perfect leak-free connection from external tubing to the microreactor (see Figs. S1.2 and S1.3 in the ESI).¹⁹ The temperature of the micromodel (T) was controlled thanks to a heating element (DBK Enclosures) put in contact with the back side of the device and associated to an Eurotherm® temperature controller. This ensures a good thermalization of the water and the CO_2 before they meet inside the pore network. Two high pressure piston pumps (ISCO®, 100DM) are used to control the upstream flow rates of CO_2 (constant flowrates mode - pump 1, Fig. 2) and the downstream pressure P_2 (constant pressure mode - pump 2, Fig. 2). The pressure drop (ΔP) across the micromodel can be determined by subtracting the outlet pressure (P_2) to the inlet pressure (P_1). The microsystem is first saturated with water and gradually pressurized to desired experimental pressures for 30 min thanks to pump 2. Pump 1 is loaded with pure CO_2 at 10 MPa and the cylinder is cooled down to 0°C to liquefy CO_2 . The CO_2 is injected into the experimental setup at constant volumetric flow rate (Q_{pump}) leading to the so-called CO_2 drainage process. In this study, two different injection flow rates were considered, corresponding to an average CO_2 velocity in the microsystem ranging from 0.04 to 0.36 m s^{-1} , depending on the physical conditions of the CO_2 (gas, liquid or supercritical). Indeed, we can define a mean CO_2 pore velocity, which is linked to the mass conservation between the pump and the microsystem and based on the density variation occurring due to temperature changes as:

$$\bar{u}_{\text{CO}_2} = \frac{Q_{\text{pump}}}{A_T \times \phi} \times \frac{\rho_{\text{pump}}}{\rho_{\mu\text{S}}} \quad (\text{Eq. 6})$$

where Q_{pump} is the volumetric flow rate given by the pump, A_T is the pore network total cross section area, i.e. $w \times d$ (m^2), ϕ is the pore networks porosity (%), ρ_{pump} is the density of the fluid inside the pump and $\rho_{\mu\text{S}}$ the one inside the microsystem. This mean CO_2 pore velocity can then be linked to the conventional Darcy velocity by:

$$u_{\text{Darcy}} = \bar{u}_{\text{CO}_2} \times \phi \quad (\text{Eq. 7})$$

The typical fluids used in the experiments consisted of deionized (DI) water and pure CO_2 . In most of the selected geological formations for the CO_2 storage at depths $> 800\text{m}$, CO_2 can reach the supercritical region ($p > 7.39 \text{ MPa}$ and $T > 31^\circ\text{C}$). Here, we have investigated five distinct conditions for the CO_2 injection, which correspond to the (p,T) values where CO_2 is a pressurized dense gas ($p = 4.5$ or 6 MPa , $T = 28^\circ\text{C}$), a liquid ($p = 8 \text{ MPa}$, $T = 28^\circ\text{C}$) or a supercritical fluid ($p = 8 \text{ MPa}$ and $T = 50^\circ\text{C}$ or 75°C). The physical properties of the fluid systems for the various (p,T) conditions considered here are

summarized in section S3 in ESI. Table 2 recapitulates the different conditions presented in this paper. The range of CO₂ flowrates and therefore the mean injection velocities (u_{CO_2}) was selected to allow fast screening while staying in the validity of the Darcy's law.

Table 2. Summary of the investigated flow and conditions characteristics.

Exp. #	P (MPa)	T (°C)	Q_{pump} ($\mu\text{L min}^{-1}$)	Micromodel	\bar{u}_{CO_2} (m s^{-1})
1	4.5	28	100	M1	0.28
2	6	28	100	M1	0.17
3	8	28	100	M1	0.04
4	8	50	100	M1	0.14
5	8	50	200	M1	0.29
6	8	75	100	M1	0.19
7	4.5	28	100	M2	0.33
8	8	28	100	M2	0.05
9	8	50	100	M2	0.17

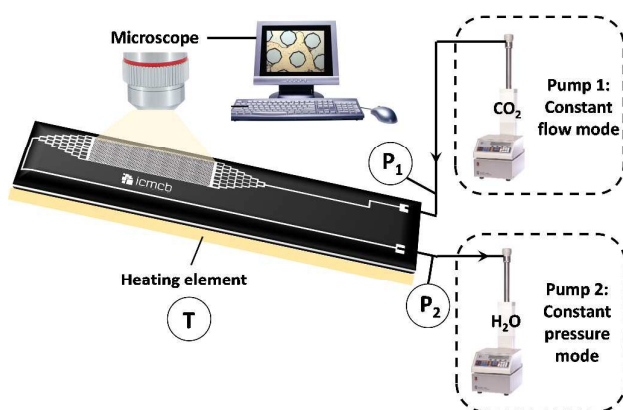


Fig. 2. Schematic view of the experimental setup developed for the investigation of CO₂ invasion in aqueous medium-saturated porous networks.

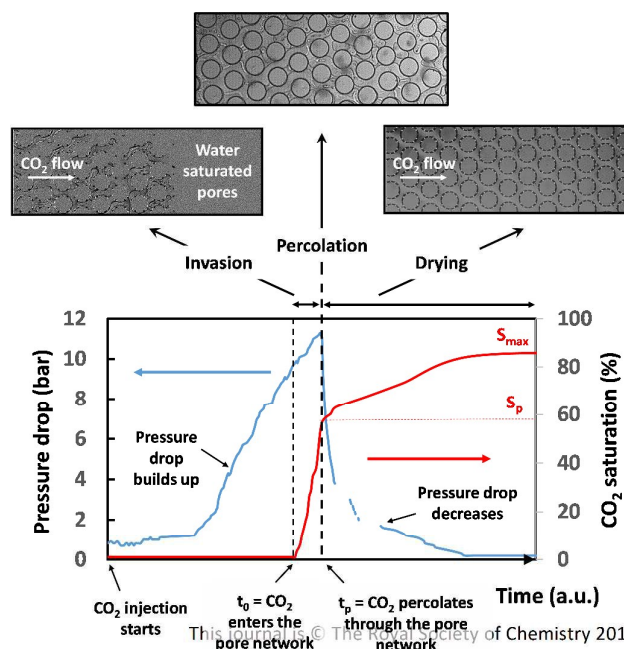
Optical system and images acquisition. The image monitoring of the water saturated micromodel was made using a Phantom® V 9.1 CMOS camera operated at 5000 fps, connected to the inverted microscope equipped with a x2.5 objective. The micromodel was placed horizontally on the isolation stage of the microscope. A homogeneous backlight (Illuminator HXP 200C – Zeiss) was placed below the chip. On the images, the water – CO₂ interfaces can be clearly seen because of the difference of refractive index (at 25°C: $n_{\text{water}} \sim 1.33$ and $1.02 < n_{CO_2} < 1.18$, depending on pressure in the range 4 – 8 MPa).³⁶ Meanwhile, the water phase appears in slight gray, while the CO₂ phase is brighter, which is primarily due to a complex combination of light scattering cross sections and geometrical optics. The images of micromodels were analyzed using the ImageJ software to quantitatively evaluate the CO₂ saturation values (S_{CO_2}). The method was first

validated by comparing the measured porosity (obtained from images with a full CO₂ saturated microsystem) and the calculated porosity (obtained by measuring the effective surface of the silicon plots). The comparison showed good agreement with errors < 2 %. The details of the method were previously reported elsewhere.²¹

Results

When CO₂ enters the pores network saturated with water, the drainage process includes three main steps, which have been identified (Fig. 3): (i) the invasion in which the CO₂ phase invades the porous medium, breaking the capillary barrier in the pore, and displacing water to occupy the pore space, which has been the most investigated process so far in the literature,^{7, 34} (ii) the percolation, which corresponds to the breakthrough time (t_p) when the CO₂ reaches the outlet of the micromodel, leaving behind some water due to a capillary forces and (iii) the drying, which corresponds to a slower elimination process in which the dry injected CO₂ vaporizes the water remaining in the pore network.

As mentioned in the introduction part, these three mechanisms can be followed with the GLoCs by measuring the pressure drop across the micromodel (classical) and the saturation curve (specific to this microfluidic tools) as a function of time (Fig. 3). When the injection of CO₂ starts, the pressure drop builds up inside the micromodels. This results from the flow of viscous water (pushed by the CO₂) within the full set-up (feeding tubing, microchannels, adaptive parts and pore network). Once the CO₂ enters in the pore network, the saturation of CO₂ increases since it replaces water in some areas of the porous medium (**Invasion step**). When CO₂ reaches the outlet of the pore network (**Percolation**), the pressure drop suddenly decreases since the low viscosity CO₂ follows a continuous flow path from the input to the output. The final step consists in a slow increase of the saturation value of CO₂ to reach a plateau (**Drying step**), which combines: (i) the water wetting film destabilization on the micromodels



walls and (ii) the drying of the residual isolated water areas.

Fig. 3. Pressure drop and CO₂ saturation as functions of time during a typical drainage process inside a micromodel. The images on the top serve at illustrating the three main mechanisms: (i) invasion, (ii) percolation and (iii) drying. Note that in our protocol, we always considered $t_0 = 0$ as the starting point for the injection time.

Note that for some particular conditions (supercritical CO₂ at temperatures $\geq 50^\circ\text{C}$), an intermediate step occurs between the percolation and the drying step, which is mostly due to some side fingering. Several information can be taken out from the saturation curves depending on the operating conditions such as: the saturation at percolation (S_p), the maximal final saturation after long injection time of 20 min (S_{max}) or the time to percolation after CO₂ enters the pore network (percolation time, $t_p - t_0 = t_p$).

In order to gain better understanding in the evolution of $S(t)$ and the values of S_p as a function of the pressure and temperature conditions, it is convenient to introduce a dimensionless number N_{eq} , which can be seen as an equivalent to the injected pore volume at the percolation time t_p in the pump conditions. N_{eq} is defined as (Eq 7):

$$N_{eq} = \frac{t_p \times Q_{pump}}{A_T \times \phi \times L} \times \frac{\rho_{pump}}{\rho_{\mu S}} = \bar{u}_{CO_2} \times \frac{t_p}{L} = \frac{\bar{u}_{CO_2}}{u_{ref}} \quad (\text{Eq. 7})$$

where t_p is the time at percolation (s), Q_{pump} is the volumetric flowrate of the CO₂ pump ($\text{m}^3 \text{s}^{-1}$), A_T is the pore network total cross section area (m^2), ϕ the porosity, L is the pore network length (m), ρ_{pump} and $\rho_{\mu S}$ are the CO₂ density in the pump and in the microsystem (kg m^{-3}), respectively. The reference velocity u_{ref} can be seen as the velocity of a fluid travelling across the pore network length (L) in a time t_p . This dimensionless number can be >1 (Table 3) oppositely to the conventional number of injected pore volumes at percolation time used when considering incompressible fluids. This can be understood because of the density variation effects in the present experiments leading to fluids dilatation and/or contraction. N_{eq} is therefore linked to the weight of fluid injected by the pump ($W_{CO_2} = Q_{pump} \times \rho_{pump} \times t_p$ in μg) rather than to the volume of fluid injected. Note that when considering compressible flow in porous media (core scale experiments), researchers generally pay much attention to gravity effects over the fluid repartition due the huge density difference between liquids and gases. In our experiments, these effects can be neglected given that we consider fluid flows in microreactors that are shallow 3D structures.

These four parameters can help comparing the influence of the operating conditions in view of optimizing the storage capacity. Note that all the experiments were repeated at least four times, demonstrating a good reproducibility for the obtained values of the parameters S_b , S_{max} , t_p , N_{eq} and W_{CO_2} .

Saturation curves. The detailed shapes of the various CO₂ saturation curves are reported in Fig. 4. The three main parameters investigated are (i) the CO₂ injection flowrate, (ii) the p and T conditions, driving the physical form of the

injected CO₂ (liquid, gas or supercritical) and (iii) the pore network geometry as a function of the injection time and/or the volume expressed as $N_p = N_{eq} \times t/t_p$ (number of equivalent pore volume). The values of t_p , N_{eq} , W_{CO_2} , S_p and S_{max} are reported in Table 3 for each experiment.

Table 3. Experimental values of t_p , N_{eq} , W_{CO_2} , S_p and S_{max} obtained from the CO₂ saturations curves for each of the investigated conditions.

Exp. #	t_p (s)	N_{eq}	W_{CO_2} (μg)	S_p (%)	S_{max} (%)
1	1.45	21.2	22.6	72	84
2	1.40	12.7	22.1	67	80
3	0.25	0.6	4.0	64	69
4	0.55	4.2	8.8	72	100
5	0.27	4.2	8.7	73	100
6	0.40	3.9	6.4	79	100
7	1.15	20.6	17.9	74	79
8	0.90	2.6	14.4	64	72
9	0.95	8.5	15.2	57	85

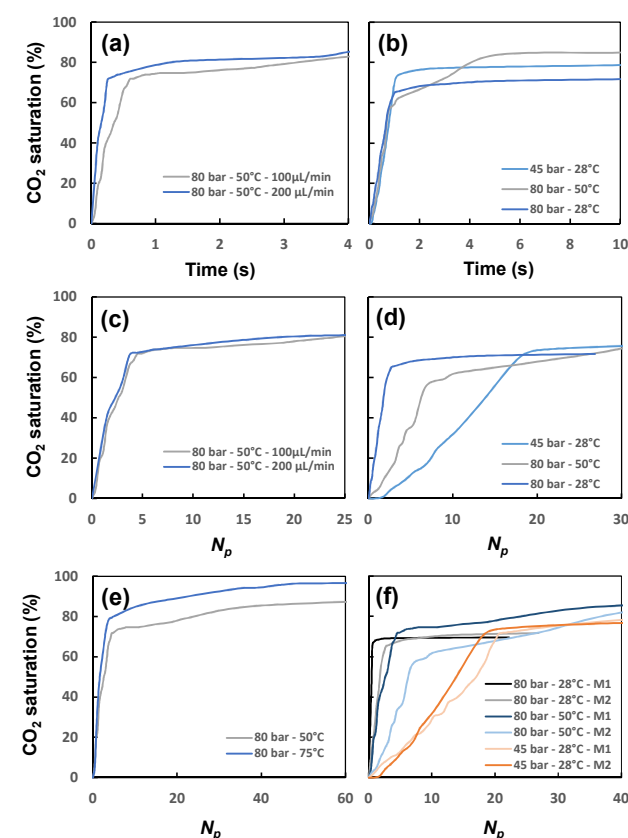


Fig. 4. CO₂ saturation for two CO₂ injection flow rates (100 and 200 $\mu\text{L min}^{-1}$) in micromodel M1 versus the injection time (exps. # 4 and 5), (b) for three (p,T) conditions ($Q_{CO_2} = 100 \mu\text{L min}^{-1}$) in micromodel M2 versus the injection time (exp. # 7 to 9), (c, d) same as (a) and (b) but versus N_p , (e) for two temperatures versus N_p (micromodel M1, $Q_{CO_2} = 100 \mu\text{L min}^{-1}$, exps. # 4 and 6) and (f) for two pore network geometry (micromodel M1 or M2) and different physical forms of CO₂ versus N_p ($Q_{CO_2} = 100 \mu\text{L min}^{-1}$, exps. # 1, 3, 4 and 7 to 9).

Invasion process. During the drainage, viscosity, wettability and capillary forces played significant roles by affecting locally the CO₂-water displacement and the subsequent CO₂ saturations in porous media. To account for all these parameters, it is often convenient to consider the phase diagram of Lenormand *et al.*³⁷ (*Log Ca* - *Log M* stability diagram) to determine the flow regime. Displacement of water by supercritical CO₂ in the case of CO₂ injection into saline aquifers typically occurs at low viscosity ratios with *log M* ranging between -1.6 and -0.7. Meanwhile, the capillary number in all our experimental conditions was calculated and *Log Ca* is ranging from -4 to -3.6 (see section S4 in ESI). Therefore, all the conditions investigated in this study are confined within a non-uniform CO₂ distribution regime,⁷ which develops as a result of unstable displacement (see Lenormand's diagram in section S5 and movie M1 in ESI).

Fig. 4-a displays the evolution of the CO₂ saturation as a function of the injection time for two different flow rates, namely: 100 and 200 $\mu\text{L min}^{-1}$ at *p* = 8 MPa and *T* = 50°C (supercritical CO₂) using the M1 GLoC. As seen from Table 3, an injection flowrate variation does not induce a strong variation neither on *S_p* (72% compared to 73%) nor on *S_{max}* (100% each) however, the breakthrough time is twice smaller (0.27s compared to 0.55s for 200 and 100 $\mu\text{L min}^{-1}$, respectively). Interestingly, by replotting the saturation value as a function of *N_p* (Fig. 4-c), one can notice that both saturation curves can almost be superimposed and the *N_{eq}* values are equal. Therefore, in these operating conditions, it can be concluded that an increase of the flow rate will only speed up the invasion process.

Fig. 4-b compares the effect of the *p* and *T* conditions (and therefore of the physical forms of CO₂: gas, liquid or supercritical) over the saturation curve as a function of the injection time. It can be seen that the percolation time looks somewhat similar in all case (*t_p* ranges from 0.90s to 1.15s, Table 3 and Fig. 4-b). Nevertheless, the variation of the CO₂ density from the pump to the GLoC induces a strong variation of *N_p* (20.6, 8.5 and 2.6 for the gas, the supercritical phase and the liquid, respectively, see Table 3 and Fig. 4-d). When the CO₂ is liquid, the density is higher and the interfacial tension between the CO₂ and water is lower, resulting in a lower capillary breakthrough pressure. We can also see that the gas phase displaces the highest quantity of water before the percolation (*S_p* = 74%), which is higher than for the liquid (*S_p* = 64%) and for the supercritical CO₂ (*S_p* = 57%). However, the saturation does not change much after percolation for both gas (4.5 MPa) and liquid (8 MPa) CO₂ at 28°C. The supercritical CO₂ (*T* = 50°C and *p* = 8 MPa) actually creates a smaller pathway to the outlet but then, a second mechanism of side fingering allows the drainage of supplementary water (see the second increase - shoulder - on Fig. 4-c from 1 to 4 s). Eventually, a drying mechanism occurs, which is more efficient for the supercritical phase, and will make the CO₂ saturation values slowly grow until *S_{max}* is reached (see discussion in section "drying mechanism").

The temperature effect (*T* = 50°C and 75°C) at constant pressure and supercritical conditions is reported on Fig 4-e. First, it can be seen that higher temperature leads to somewhat shorter times to breakthrough and decreases the *N_{eq}* values (*t_p* = 0.4s and *N_{eq}* = 3.9 at 75°C, compared to *t_p* = 0.55s and *N_{eq}* = 4.2 at 50°C). Additionally, although the saturation at percolation is higher for higher temperature (*S_p* = 79% for 75°C and *S_p* = 72% for 50°C), this initial trends is erased during the drying process since eventually *S_{max}* is the same for both conditions (100%) at long injection times. Overall, a higher temperature only seems to provide a better initial invasion capability.

Eventually, Fig. 4-f displays the CO₂ saturation as a function of *N_p* for the two different micromodels (M1 and M2) for the three different physical forms of CO₂ (*Q_{CO2}* = 100 $\mu\text{L min}^{-1}$). As seen, whatever the considered micromodel, the same trends is observed, *i.e.* the gaseous CO₂ required higher values of *N_p* to reach the percolation than the liquid or the supercritical CO₂. Then, it can be noticed that a decrease of the micromodel depth (and therefore an increase of the final total pore volume (*V_T* × ϕ) from 0.81 μL to 0.98 μL for M1 and M2, respectively) results in a decreasing *N_{eq}* value (and thus a lower *t_p*) for liquid and supercritical CO₂. The capillary pressure in M1 is indeed lower and easier to break (the meniscus radius being higher), leading to a wider pathway, which can occupy a higher area in the micromodel. This trend is far less pronounced for gaseous CO₂ for which the saturation curves as a function of the injected pore volume in the M1 micromodel is indeed exhibiting a greater slope in the beginning of the injection (similar to liquid and supercritical CO₂), before an inversion of the behaviour at larger *N_p* values (Fig. 4-f). This could be explained by a smaller hydrodynamic resistance through the porous medium when considering the non-viscous gas phase, meaning the fluid pathway is less influenced by the geometry in this particular case. Additionally, from the data available on Table 3, it can be noticed that the *S_p* values (for gas and liquid) are similar for the M1 and M2 micromodel (72% and 64%, respectively compared to 74% and 64%, respectively). Conversely, supercritical CO₂ leads to a different behaviour since *S_p* values are different depending on the considered micromodel geometry (for M1, *S_p* = 72%, whereas for M2, *S_p* = 57%). Indeed, the initial pathway is smaller for M2 than for M1, because of the higher capillary pressure, leading to a smaller value of *S_p*. Then, the side fingering process coupled to drying occurs leading to an increase of 28% of the saturation value in both cases (*S_{max}* = 100% for M1 and *S_{max}* = 85% for M2).

Percolation / capillary trapping. Once CO₂ percolates through the pore network, some water is left behind due to capillary trapping. Indeed, capillary forces can locally create some flow barriers preventing the CO₂ to penetrate the pore throat of some areas during the invasion process. The capillary entry pressure *p_e* being proportional to the interfacial forces and inversely proportional to the size of pore structure, the CO₂ first enters the pore body before being stopped at a pore throat unless the flow pressure overcomes *p_e*. In addition, the CO₂ plume tail can also be snapped off by capillary forces

resulting in disconnected CO₂ saturated areas (see Fig. 5-a). The water left behind typically arranges in three main “structures”, which were identified during the experiments: pools, bridges and domes (Fig. 5).

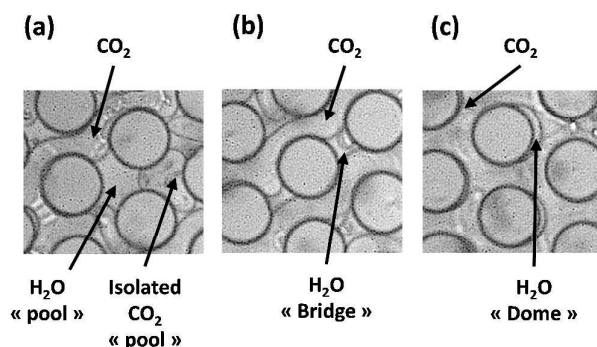


Fig. 5. Typical configurations observed for the left-behind water in the pore network after CO₂ percolation: (a) pools with isolated CO₂ saturated areas, (b) bridges and (c) domes.

First, water pool connects three or more neighbouring plots, occupying multiple pore bodies (Fig. 5-a). Once a first snapping off phenomena occurs, the water pool can change to a water bridge between pore throats (Fig. 5-b). This configuration connects two hydrophilic neighbouring plots through interfacial meniscus of similar concave curvature governed by the shortest distance between the plots. Some hydrophilic silica plots appear surrounded by water “domes” (Fig. 5-c). Although it is understandable that water films are easy to form in a hydrophilic porous medium, it is less straightforward to explain the formation of water domes with inverse curvature partially surrounding some silica plot. Indeed, such structures required surface heterogeneities for the triple line (water/CO₂/solid) to be stabilized, which are provided by the silicon wet etching process. The energy generated by the triple line contact can therefore explain the inverse curvature of the domes. Overall, such domes structures ensue from a mechanism similar to the one allowing water to rise above the edge of a full glass, resulting in a concave meniscus, due to surface tension effects. Therefore, the roughness of the silica plots (depending on the microfabrication procedure) can greatly affect the formation of these domes. Hence, it appears that when considering heterogeneous pore network (typically encountered in real geological reservoir), such wetting films could easily form, therefore impacting strongly the final saturation values of CO₂ in the porous medium at percolation. In addition, the dissolution of CO₂ in water decreases the water pH (from 6-7 to ~3 depending on the operating conditions), therefore weakening the relative affinity of water to the silica surface.³⁸ These changes in affinity trend to increase the wetting contact angle of CO₂ and weaken the stability of the water domes.

For all the cases illustrated above, the two-phase distributions correspond to a fraction of residual water entrapped in the

pore network. Such a situation demonstrates the decrease of the effective porosity of the pore network, and consequently, the reduction of the stored CO₂ quantity. Investigating these mechanisms of CO₂ invasion at pore scale in real conditions of the geological formation is then of primary importance for the CO₂ geological storage. Indeed, these different shapes identified Fig. 6 may have impacts on process occurring primarily in the wetting phase, such as geochemical reaction between dissolved carbonates and aquifer materials, including dissolution and precipitation of minerals that occur in the brine and evaporation of the brine resulting in formation dry-out.

Drying mechanism. Contrary to immiscible oil/water two phase flow in porous medium, which were mostly investigated so far for Enhanced Oil Recovery purposes,¹¹ the case of CO₂-water is somewhat different since both fluids exhibit a small miscibility in each other, which depends on the *p* and *T* conditions. Therefore, the system does not reach equilibrium after percolation. When considering long injection times, an additional mechanism occurs: the remaining water is dried out by the flow of fresh CO₂ entering the pore network. These types of mechanisms were previously studied when considering the drying of liquid saturated micromodels or porous media.³⁹⁻⁴² In our case, two steps have been identified for this process: (i) the water wetting film destabilization and its further dewetting, and (ii) the drying of the remaining “bulk” water saturated areas.

The first step can be clearly identified in all the investigated conditions (Fig. 6) with the visualization of film thickness variations and further breaking. The destabilization of the water film occurs at different times after the percolation, depending on the experimental conditions. The upper (Pyrex side) and lower (silicon side) films of water are subjected to stresses from the combined effects of the CO₂ flow passing between them, creating instabilities and the slow dissolution of H₂O in the CO₂ flow. The film destabilization generates holes and droplets structures visible on Fig. 6 on the Pyrex side (see movie M2 in ESI). Given the random organization of holes in the film, this mechanism can be assimilated to heterogeneous nucleation dewetting.^{43, 44} The volume of water stabilized as a wetting film was not taken into account in this study since it remains negligible compared to the overall volume of water in the bulk. Although the film thickness (*h*) was not measured quantitatively, it is possible to estimate it with the Bretherton's law for determining the film thickness of a wetting film left behind in segmented flow inside a cylindrical capillary:⁴⁵

$$h \sim r \times Ca^{2/3} \quad (\text{Eq. 8})$$

With *r* the capillary radius and *Ca* the capillary number, which can be obtained from Eq. 3. Using Eq. 8, it is possible to estimate the value of the water film thickness in the range 50 – 100 nm depending on the pressure and temperature conditions. Note that theoretical models have been recently developed for accessing more precise calculations of the actual volume of droplets in various microfluidics geometries from 2D top view images,⁴⁶ which could be adapted to the current porous network microsystems. Interestingly, such thin films increase the surface exchange area

PAPER

Lab Chip

between CO₂ and water and potentially enhance phenomena like dissolution processes or chemical reaction.

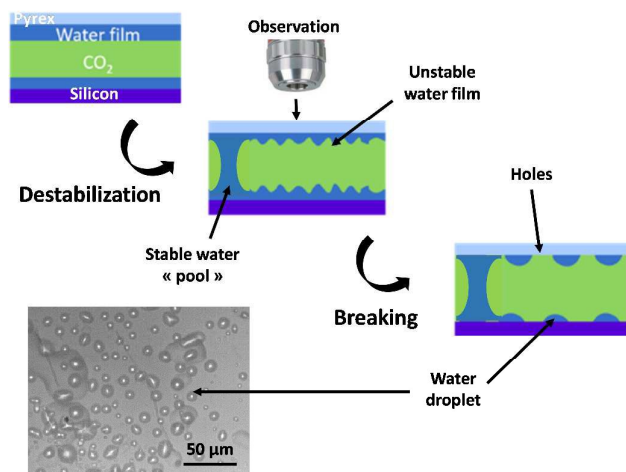
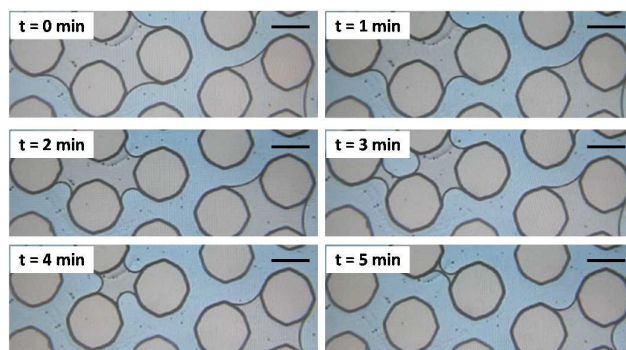


Fig. 6. Scheme of the water wetting film destabilization and optical characterization of water droplets on the Pyrex side.

Once the water wetting film is broken, the bulk water saturated areas are slowly dried out through a solubilisation mechanism (Fig. 7 and movie M3 in the ESI). In particular, it can be seen that (i) the surface area occupied by the water pools slowly decreases leading to the formation of bridges and (ii) the contact angle at the interface between the water and the CO₂ slightly increases with the injection time. The solubility of water in CO₂ is quite small in the considered experimental conditions, although this is compensated by fast mass transfer process at micro scale coupled to continuous feeding of the microsystem with fresh dry CO₂. Additionally, the menisci generated by capillary pressure at the interface between the two phases increase the contact area available for water dissolution, therefore enhancing the drying process. Meanwhile, the dissolution of CO₂ into water reduces the stability of the water wetting dome, pool and bridges. Therefore, the drying mechanism increases the saturation of CO₂ behind the displacement front, as seen from the comparison between the values of S_p and S_{max} in all the



investigated conditions (Table 3).

Fig. 7. Evolution of an area of the porous medium after percolation as a function of the CO₂ injection time showing the drying the water pools (experiment performed at $p = 8$ MPa, $T = 50^\circ\text{C}$, $Q_{\text{CO}_2} = 50 \mu\text{L min}^{-1}$). The scale bar is $200 \mu\text{m}$.

The dissolution kinetics depend on the experimental conditions. In particular, it was found out that the drying mechanism was faster at 75°C than at 50°C (exps. #4 and 6), although both conditions lead to a final CO₂ saturation (S_{max}) of 100% after 20 min of injection (see section S6 in ESI). Although porosity should be the main parameter to control the drying process, which occurs through interface dissolution, the temperature effect can be explained by an increasing solubility of water in CO₂ with temperature at 8 MPa, namely: $3.4 \cdot 10^{-3} \text{ mol}^{-1}$ at 50°C and $8.3 \cdot 10^{-3} \text{ mol}^{-1}$ at 75°C (see Fig. S7 in the ESI),⁴⁷ which can speed up the drying process.

Conclusion

A series of displacement experiments was conducted using two different geological labs on chip in order to investigate the different mechanisms involved during the drainage of a water saturated porous medium by CO₂. Various experimental parameters were studied, in particular the (p, T) conditions (and therefore three different physical forms of CO₂: gas, liquid and supercritical), the micromodels geometry and the injection flowrate. Thanks to optical characterization coupled to images processing, the displacement process and the CO₂ saturation curves as a function of time (or the injected pore volume) were determined. Three main mechanisms were observed during the CO₂ injection, namely: invasion, percolation and drying.

It was shown that the invasion step is largely dependent on the p and T conditions, liquid CO₂ percolates first, while supercritical CO₂ lead to the highest CO₂ saturation. After percolation, it was observed that some water is left behind and occupy multiple pore bodies arranged in various structures between the silicon plots: pools, bridges or domes. Eventually, the remaining water is partially or totally dried out by the flow of fresh CO₂ through a solubilization process.

These observations performed using Geological Labs on Chip (GLOCs - micromodels) at pore scale open ways to determine qualitatively what could be expected at larger scales depending on the operating conditions, by feeding the numerical models. Further works will consider the effect of heterogeneities (porosity, wettability) and geochemical reactions (brine composition, reactive surface materials) thanks to the implementation of other characterization techniques such as in situ X-Rays.⁴⁸

Acknowledgements

We authors wish to thank the ANR for funding this work through the CGSμLab-ANR-12-SEED-0001 project

Notes and references

1. R. K. Pachauri, *Climate Change 2014 Synthesis Report*, 2014.
2. J. Orr, F. M., *Journal of Petroleum Technology*, 2004, **56**, 90-97.
3. C. M. White, D. H. Smith, K. L. Jones, A. L. Goodman, S. A. Jikich, R. B. LaCount, S. B. DuBose, E. Ozdemir, B. I. Morsi and K. T. Schroeder, *Energy & Fuels*, 2005, **19**, 659-724.
4. S. M. V. Gilfillan, B. S. Lollar, G. Holland, D. Blagburn, S. Stevens, M. Schoell, M. Cassidy, Z. Ding, Z. Zhou, G. Lacrampe-Couloume and C. J. Ballentine, *Nature*, 2009, **458**, 614-618.
5. E. N. Mbia, P. Frykman, C. M. Nielsen, I. L. Fabricius, G. E. Pickup and C. Bernstone, *International Journal of Greenhouse Gas Control*, 2014, **22**, 139-153.
6. C. Hermanrud, T. Andresen, O. Eiken, H. Hansen, A. Janbu, J. Lippard, H. N. Bolås, T. H. Simmenes, G. M. G. Teige and S. Østmo, *Energy Procedia*, 2009, **1**, 1997-2004.
7. C. Zhang, M. Oostrom, T. W. Wietsma, J. W. Grate and M. G. Warner, *Energy & Fuels*, 2011, **25**, 3493-3505.
8. R. Juanes, E. J. Spiteri, F. M. Orr and M. J. Blunt, *Water Resources Research*, 2006, **42**, W12418.
9. W. A. Ambrose, S. Lakshminarasimhan, M. H. Holtz, V. Núñez-López, S. D. Hovorka and I. Duncan, *Environmental Geology*, 2007, **54**, 1619-1633.
10. M. A. Hesse and A. W. Woods, *Geophysical Research Letters*, 2010, **37**, L01403.
11. C. Cottin, H. Bodiguel and A. Colin, *Physical Review E*, 2010, **82**, 046315.
12. J.-C. Perrin and S. Benson, *Transport in Porous Media*, 2009, **82**, 93-109.
13. J. El-Ali, P. K. Sorger and K. F. Jensen, *Nature*, 2006, **442**, 403-411.
14. Y. Zheng, J. Nguyen, Y. Wei and Y. Sun, *Lab on a Chip*, 2013, **13**, 2464-2483.
15. R. L. Hartman and K. F. Jensen, *Lab on a Chip*, 2009, **9**, 2495-2507.
16. K. F. Jensen, B. J. Reizman and S. G. Newman, *Lab on a Chip*, 2014, **14**, 3206-3212.
17. N. J. W. Straathof, Y. Su, V. Hessel and T. Noel, *Nat. Protocols*, 2016, **11**, 10-21.
18. S. Marre and K. F. Jensen, *Chemical Society Reviews*, 2010, **39**, 1183-1202.
19. S. Marre, A. Adamo, S. Basak, C. Aymonier and K. F. Jensen, *Industrial & Engineering Chemistry Research*, 2010, **49**, 11310-11320.
20. B. Pinho, S. Girardon, F. Bazer-Bachi, G. Bergeot, S. Marre and C. Aymonier, *Lab on a Chip*, 2014, **14**, 3843-3849.
21. M. Buchgraber, A. R. Kovscek and L. M. Castanier, *Transport in Porous Media*, 2012, **95**, 647-668.
22. N. S. Kumar Gunda, B. Bera, N. K. Karadimitriou, S. K. Mitra and S. M. Hassanizadeh, *Lab on a Chip*, 2011, **11**, 3785-3792.
23. L. Zuo, C. Zhang, R. W. Falta and S. M. Benson, *Advances in Water Resources*, 2013, **53**, 188-197.
24. M. Soroush, D. Wessel-Berg, O. Torsaeter and J. Kleppe, *Energy Science & Engineering*, 2014, **2**, 149-163.
25. W. Song, T. W. de Haas, H. Fadaei and D. Sinton, *Lab on a Chip*, 2014, **14**, 4382-4390.
26. V. A. Lifton, *Lab on a Chip*, 2016, **16**, 1777-1796.
27. N. Liu, C. Aymonier, C. Lecoutre, Y. Garrabos and S. Marre, *Chemical Physics Letters*, 2012, **551**, 139-143.
28. C. Zhang, K. Dehoff, N. Hess, M. Oostrom, T. W. Wietsma, A. J. Valocchi, B. W. Fouke and C. J. Werth, *Environmental Science & Technology*, 2010, **44**, 7833-7838.
29. T. W. Willingham, C. J. Werth and A. J. Valocchi, *Environmental Science & Technology*, 2008, **42**, 3185-3193.
30. CGS_μLab project - ANR SEED 2012 <http://www-anr-cgsmicrolab.cnrs.fr/>.
31. A. L. Herring, L. Andersson, D. L. Newell, J. W. Carey and D. Wildenschild, *International Journal of Greenhouse Gas Control*, 2014, **25**, 93-101.
32. R. Couto, S. Chambon, C. Aymonier, E. Mignard, B. Pavageau, A. Erriguible and S. Marre, *Chemical Communications*, 2015, **51**, 1008-1011.
33. N. K. Karadimitriou, S. M. Hassanizadeh, V. Joekar-Niasar and P. J. Kleingeld, *Water Resources Research*, 2014, **50**, 8125-8140.
34. C. Zhang, M. Oostrom, J. W. Grate, T. W. Wietsma and M. G. Warner, *Environmental Science & Technology*, 2011, **45**, 7581-7588.
35. C. Chalbaud, M. Robin, J.-M. Lombard, H. Bertin and P. Egermann, *Oil Gas Sci. Technol. – Rev. IFP*, 2010, **65**, 541-555.
36. A. Michels and J. Hamers, *Physica*, 1937, **4**, 995-1006.
37. R. Lenormand, *Journal of Physics: Condensed Matter*, 1990, **2**, SA79.
38. Y. Kim, J. Wan, T. J. Kneafsey and T. K. Tokunaga, *Environmental Science & Technology*, 2012, **46**, 4228-4235.
39. Y. Peysson, M. Fleury and V. Blázquez-Pascual, *Transport in Porous Media*, 2011, **90**, 1001-1016.
40. Y. Peysson, B. Bazin, C. Magnier, E. Kohler and S. Youssef, *Energy Procedia*, 2011, **4**, 4387-4394.
41. Y. Peysson, L. André and M. Azaroual, *International Journal of Greenhouse Gas Control*, 2014, **22**, 291-300.
42. M. Prat, *Chemical Engineering Journal*, 2002, **86**, 153-164.
43. R. V. Craster and O. K. Matar, *Reviews of Modern Physics*, 2009, **81**, 1131-1198.
44. R. W. Aul and W. L. Olbricht, *Journal of Fluid Mechanics*, 1990, **215**, 585-599.
45. P. Aussillous and D. Quéré, *Physics of Fluids*, 2000, **12**, 2367-2371.
46. M. Musterd, V. van Steijn, C. R. Kleijn and M. T. Kreutzer, *RSC Advances*, 2015, **5**, 16042-16049.
47. N. Spycher, K. Pruess and J. Ennis-King, *Geochimica et Cosmochimica Acta*, 2003, **67**, 3015-3031.
48. T. Beuvier, E. A. C. Panduro, P. Kwasniewski, S. Marre, C. Lecoutre, Y. Garrabos, C. Aymonier, B. Calvignac and A. Gibaud, *Lab on a Chip*, 2015, **15**, 2002-2008.